



A CoFe₂O₄/graphene nanohybrid as an efficient bi-functional electrocatalyst for oxygen reduction and oxygen evolution

Weyong Bian^a, Zhenrong Yang^a, Peter Strasser^b, Ruizhi Yang^{a,*}

^a School of Physical Science and Technology, School of Energy, Soochow University, Suzhou, Jiangsu 215006, China

^b The Electrochemical Energy, Catalysis, and Materials Science Laboratory, Department of Chemistry, Chemical Engineering Division, Technical University Berlin, 10623 Berlin, Germany

HIGHLIGHTS

- A CoFe₂O₄/graphene nanohybrid is facilely synthesized.
- CoFe₂O₄/graphene nanohybrid is an efficient bi-functional electrocatalyst for the ORR and the OER.
- CoFe₂O₄/graphene nanohybrid could be used as a potential catalyst for metal–air batteries.

ARTICLE INFO

Article history:

Received 28 August 2013

Received in revised form

25 October 2013

Accepted 12 November 2013

Available online 20 November 2013

Keywords:

Bi-functional electrocatalyst
Oxygen reduction reaction
Oxygen evolution reaction
Spinel oxide/graphene nanohybrid

ABSTRACT

Development of efficient electrocatalysts for the oxygen reduction reaction (ORR) and the oxygen evolution reaction (OER) remain key issues for the commercialization of fuel cells and metal–air batteries. In this study, A CoFe₂O₄/graphene nanohybrid is facilely synthesized via a two-step process and applied as an electrocatalyst for the ORR and the OER. The as-prepared CoFe₂O₄/graphene nanohybrid demonstrates excellent catalytic activity for the ORR. At the same mass loading, the Tafel slope of CoFe₂O₄/graphene electrocatalyst for the ORR is comparable to that of the commercial Pt/C (20 wt% Pt on Vulcan XC-72, Johnson Matthey). The ORR on CoFe₂O₄/graphene mainly favours a direct 4e[−] reaction pathway. The CoFe₂O₄/graphene nanohybrid also affords high catalytic activity for the OER. The chronoamperometric tests show that CoFe₂O₄/graphene catalyst exhibits excellent stability for both the ORR and the OER, outperforming the commercial Pt/C. The high electrocatalytic activity and durability of CoFe₂O₄/graphene nanohybrid are attributed to the strong coupling between CoFe₂O₄ nanoparticles and graphene.

© 2013 Elsevier B.V. All rights reserved.

1. Introduction

Electrocatalytic oxygen reduction reaction (ORR) and oxygen evolution reaction (OER) play critical roles in the development of fuel cells and metal–air batteries, which are promising technologies for portable, residential and especially transportation applications [1–4]. The slow kinetics of the ORR and the OER at the cathode limits the efficiency of fuel cells and metal–air batteries [1,5–8]. Platinum-based materials are known to be the most active electrocatalysts for the ORR and the OER. However, the high cost and scarcity of Pt hinders the widespread commercialization of fuel cells and metal–air batteries.

Research efforts have been focused on replacing Pt with inexpensive materials. Mixed valence oxides of transition metals with a spinel structure have attracted much attention due to their high

abundance, low cost, environmental friendliness and considerable catalytic activity for the ORR and OER [9–13]. More specifically, cobaltite spinel oxides M_xCo_{3−x}O₄ (M = Co, Ni, Mn, Cu, Li) have been shown as promising electrocatalysts for the ORR (M = Co, Ni, Mn) and the OER (M = Co, Ni, Cu, Mn, Li) [9–12,14–17]. Cheng et al. [10] have reported that nano-crystalline spinels of Co_xMn_{3−x}O₄ prepared by a rapid room-temperature synthesis method exhibited considerable catalytic activities for both the ORR and the OER. High electrocatalytic activities of Cu_xCo_{3−x}O₄ for the ORR and the OER have also been reported by Koninck et al. [14,15]. Recently, Yuan et al. reported the use of Ni_xCo_{3−x}O₄ spinel oxide as a bi-functional air electrode for zinc–air batteries [16]. Although cobaltite spinel oxides have been widely investigated as electrocatalysts for the ORR and the OER, the electrocatalytic activities of M_xCo_{3−x}O₄ with M = Fe for the ORR and the OER are still seldom reported.

In order to obtain good catalytic activity, spinel oxides are usually attached to or supported on a conducting surface (like carbon) to assure fast electron transport since this type of oxides is a semiconductor. High electrical conductivity, chemical stability,

* Corresponding author. Tel.: +86 512 65221519.

E-mail address: yangrz@suda.edu.cn (R. Yang).

large surface area and open porous structure of graphene sheets [18–20] makes it an excellent substrate for spinel oxides. $\text{Co}_3\text{O}_4/\text{graphene}$ [11], $\text{MnCo}_2\text{O}_4/\text{graphene}$ [12,13], $\text{NiCo}_2\text{O}_4/\text{graphene}$ [21] have been reported to be promising bi-functional electrocatalysts for the ORR and the OER. In this work, we report the synthesis of $\text{CoFe}_2\text{O}_4/\text{graphene}$ nanohybrid as an efficient bi-functional electrocatalyst for the ORR and the OER. To the best of our knowledge, few studies on the preparation and catalytic activity of $\text{CoFe}_2\text{O}_4/\text{graphene}$ nanohybrid have been reported so far. Laouini et al. [22,23] and Cartaxo et al. [24] studied the electrochemical behaviour of CoFe_2O_4 , electrocatalytic activity of which has not been reported. The electrocatalytic activities of the as-synthesized $\text{CoFe}_2\text{O}_4/\text{graphene}$ nanohybrid for the ORR and the OER in alkaline media have been studied by using a rotating ring-disk electrode (RRDE) technique. The as-synthesized $\text{CoFe}_2\text{O}_4/\text{graphene}$ nanohybrid exhibited high electrocatalytic activities for both the ORR and the OER with long-term stability in basic media, outperforming CoFe_2O_4 and graphene, respectively.

2. Experimental

2.1. Sample preparation

Graphene oxide (GO) is synthesized from natural graphite flakes by a modified Hummers' method as described elsewhere [11,25]. GO was collected from the aqueous solution by centrifugation followed by lyophilization. 10 mg of the GO was dispersed in 30 ml of anhydrous ethanol. For the synthesis of $\text{CoFe}_2\text{O}_4/\text{graphene}$, 1 ml of 0.2 M $\text{Fe}(\text{NO}_3)_3 \cdot 9\text{H}_2\text{O}$ and 0.5 ml of 0.2 M $\text{Co}(\text{NO}_3)_2 \cdot 6\text{H}_2\text{O}$ ($\geq 99.0\%$, Guoyao Chemical Reagent Co. Ltd.) aqueous solution was added to the above GO ethanol suspension, followed by the addition of 2.50 ml of NH_4OH at room temperature. The mixture was stirred at 80 °C for 12 h and then transferred to a 50 ml autoclave, sealed and heated at 180 °C for 5 h. After the autoclave is cooled to room temperature, the precipitate is collected by centrifugation and washed with ethanol and deionized water to remove any impurities. The final product was obtained after lyophilization. This hydrothermal step also reduced GO to rGO and the samples obtained were abbreviated to $\text{CoFe}_2\text{O}_4/\text{rGO}$. CoFe_2O_4 and rGO were also prepared with the same procedure for comparison.

2.2. Physical characterizations

The crystal structure of the sample was examined with X-ray diffraction (XRD) using a Bede D1 X-ray diffractometer (UK, Bede Scientific Ltd.; $\text{Cu K}\alpha$ radiation; operated at 40 kV, 45 mA; $\lambda = 0.15418$ nm), the diffraction angle ranging from 10° to 80° with a step of 0.02° and a rate of 1.2° min⁻¹.

Surface analysis of the samples was performed with a SSI (Surface Science Instruments) X-ray photoelectron spectroscopy (XPS) spectrometer equipped with a hemispherical analyzer and using a monochromatized Al $\text{K}\alpha$ (1486 eV) source with a 250×1000 μm illumination spot. The measurement parameters were as follows: 20 eV pass energy, 0.1 eV energy increments. The spectra were corrected for the background using the Shirley approach [26] and the composition of the films was determined by measuring the ratio of Co 2p to Fe 2p intensities (integrated peak area) normalized by their respective sensitivity factors [27].

The specific surface area and the pore structure of the samples were analyzed by adsorption/desorption measurements of nitrogen at 77 K (Quantachrome, QuadraSorb SI). Prior to measurements, the samples were degassed at 250 °C overnight under vacuum. Surface area was calculated by Brunauer–Emmett–Teller (BET) method.

Pore size distributions were calculated using Barrett–Joyner–Halenda (BJH) method.

The morphology and microstructure of the synthesized sample were characterized by a transmission electron microscope (TEM, TecnaiG220 operating at 200 kV).

The amount of CoFe_2O_4 in $\text{CoFe}_2\text{O}_4/\text{rGO}$ was measured with thermogravimetric analysis (TGA, PerkinElmer TGA7), which was calibrated with calcium oxalate.

2.3. Electrochemical measurements

Inks of the catalyst samples for $\text{CoFe}_2\text{O}_4/\text{rGO}$ (the amount of CoFe_2O_4 in the composite was determined to be 70 wt%), $\text{CoFe}_2\text{O}_4 + \text{rGO}$ mixture (the ratio of CoFe_2O_4 to rGO is 70:30 by weight), rGO and CoFe_2O_4 (mixed with acetylene black (AB), the ratio of CoFe_2O_4 to AB is 70:30 by weight) were prepared by mixing 10 mg of powder, 5 μl of Nafion solution (5 wt% from Aldrich), and 350 μl of ethanol, followed by ultrasonication for 40 min. Seven μl of ink was pipetted onto a glassy carbon (GC) disk resulting in a powder loading of 1006 $\mu\text{g cm}^{-2}$. The same powder loading was used for commercial Pt/C (20 wt% Pt on Vulcan XC-72, Johnson Matthey) for comparison.

The electrocatalytic activity for the ORR of the samples on the GC disks was studied with the rotating ring-disk electrode (RRDE) technique using a Pine electrochemical system (AFMSRX rotator, and AFCBP1 bipotentiostat). The RRDE electrode consisted of a catalyst-coated GC disk (5 mm diameter, 0.196 cm² of geometric surface area) surrounded by a Pt ring (0.125 cm² of geometric surface area). The electrochemical measurements were conducted in a standard three-electrode electrochemical cell at room temperature. A Pt-foil was used as the counter electrode, and a Ag/AgCl (3 M Cl⁻, Cypress) reference electrode was used in a double-junction reference chamber. The electrolyte was 0.1 M KOH solution prepared from ultrapure water (Millipore, 18.2 M Ω cm). The working electrodes were the catalyst film-coated GC disks mounted in a disk-interchangeable rotating disk electrode (RDE, Pine Instruments).

The electrolyte was deaerated by purging high-purity Ar gas into the electrolyte for at least 30 min before each electrochemical measurement. The samples on the GC disks were first electrochemically cleaned by sweeping the potential in the range between -0.9 and 0 V (vs. Ag/AgCl) at 50 mV s⁻¹ in an Ar-saturated 0.1 M KOH solution until steady state cyclic voltammograms (CV) were obtained. For each catalyst tested, a CV was first collected in Ar-saturated 0.1 M KOH solution from -0.9 to 0 V at 10 mV s⁻¹ to determine the non-Faradaic current.

For the ORR test, the electrolyte was purged with high-purity O₂ gas for at least 30 min to ensure O₂ saturation. Linear sweep voltammetry (LSV) measurements during oxygen reduction were performed in O₂-saturated 0.1 M KOH by sweeping the potential from 0 V cathodically to -0.8 V at 10 mV s⁻¹ with the electrode rotated at 400, 900, 1600 and 2500 rpm and O₂ gas purged into the solution at a flow rate of 25 sccm through a 2 μm fritted tube (Ace Glass). Note that the LSV measurements on Pt/C were performed by sweeping the potential from -0.8 V anodically to 0 V at 10 mV s⁻¹ to avoid the initial oxidation of Pt surface at high potential [28,29]. The faradaic current density, i.e., the current due to the oxygen reduction alone, was obtained by subtracting the capacitive current (the current measured from the CV under Ar) from the ORR data and then normalized by the geometric surface area,

$$j = -(j_{\text{ORR}} - j_{\text{capacitive, Ar-CV}}) / S_{\text{Ageo}} \quad (1)$$

The kinetic current density for the ORR was derived from the Koutecky–Levich equation:

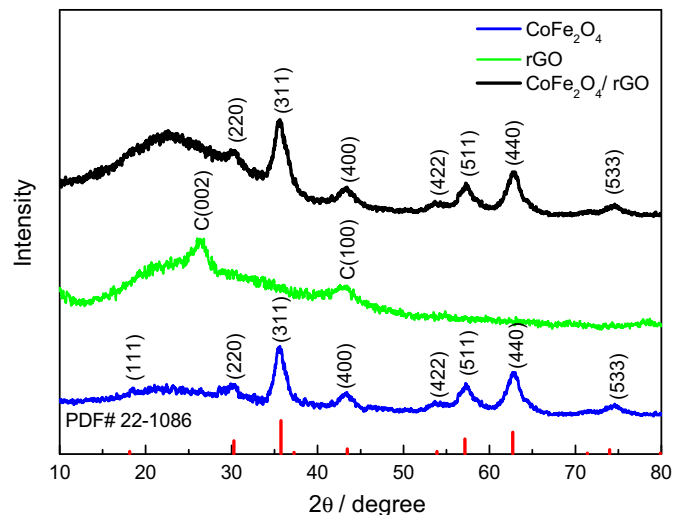


Fig. 1. XRD patterns of CoFe₂O₄, rGO and CoFe₂O₄/rGO nanohybrid.

$$1/j = 1/j_k + 1/j_d = 1/j_k + 1/(B\omega^{1/2}), \quad (2)$$

where j is the measured disk current density; j_k and j_d are the kinetic and diffusion limiting current densities, respectively;

B is the so-called “B-factor”, which is given by the following equation:

$$B = 0.62nFD_{O_2}^{2/3}v^{-1/6}C_{O_2}, \quad (3)$$

where n is the apparent number of electrons transferred in the reaction, F is the Faraday constant ($96,485 \text{ C mol}^{-1}$), D_{O_2} is the diffusion coefficient of O_2 ($D_{O_2} = 1.86 \times 10^{-5} \text{ cm}^2 \text{ s}^{-1}$), v is the kinetic viscosity of the solution ($v = 0.01 \text{ cm}^2 \text{ s}^{-1}$), C_{O_2} is the concentration of O_2 dissolved in electrolyte ($C_{O_2} = 1.21 \times 10^{-6} \text{ mol cm}^{-3}$) [28,30], and ω is the electrode rotation speed. The ohmic resistances in the electrode contacts for the investigated samples were included in the corrections.

For all the RRDE measurements, the ring potential was held at 0.5 V vs. Ag/AgCl in order to oxidize any H_2O_2 produced in alkaline solution [31]. The % HO_2^- produced in alkaline solution was calculated using the following equation [13,32,33].

$$\%HO_2^- = 100 \frac{2I_R/N}{I_D + (I_R/N)}, \quad (4)$$

where I_D is the Faradaic current at the disk, I_R is the Faradaic current at the ring, and $N = 0.22$ is the disk electrode collection efficiency.

For the OER test, the working electrode was scanned from 0 to 1.0 V vs. Ag/AgCl at a scan rate of 10 mV s^{-1} in a N_2 -saturated electrolyte with the electrode rotated at 1600 rpm to spin off the oxygen evolved during voltammetry testing.

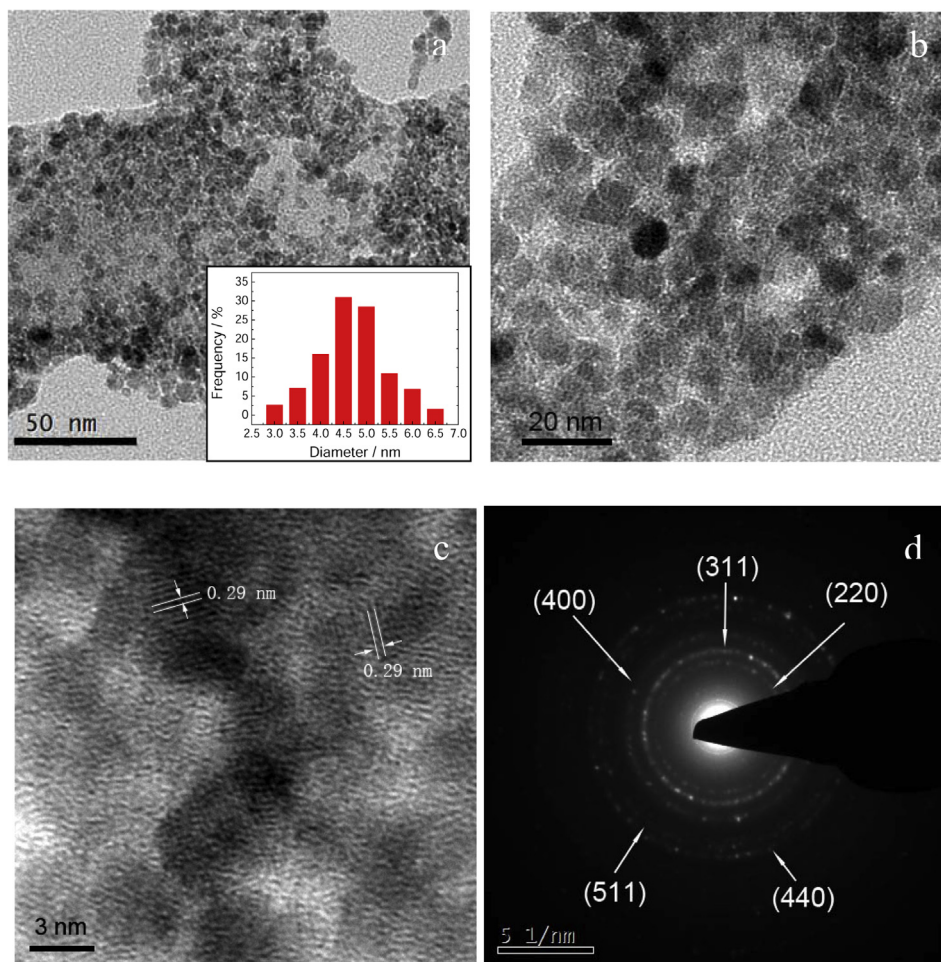


Fig. 2. TEM images of CoFe₂O₄/rGO nanohybrid with different magnifications (a) and (b); high-resolution TEM image of CoFe₂O₄/rGO (c); selected area electron diffraction (SAED) pattern of CoFe₂O₄/rGO (d). Inset of (a): Particle size distribution of CoFe₂O₄ nanoparticles in CoFe₂O₄/rGO nanohybrid.

3. Results and discussion

3.1. Structure of $\text{CoFe}_2\text{O}_4/\text{rGO}$ nanohybrid

Fig. 1 shows the X-ray diffraction (XRD) profile of the $\text{CoFe}_2\text{O}_4/\text{rGO}$, the XRD profiles of CoFe_2O_4 and rGO are also included for comparison. The characteristic peaks in $\text{CoFe}_2\text{O}_4/\text{rGO}$ can be well indexed as cubic spinel phase (PDF#22-1086) except the broad peak at around 23° corresponding to (002) peak of carbon in rGO. The average crystallite size of the CoFe_2O_4 particles is estimated to be 4.9 nm for $\text{CoFe}_2\text{O}_4/\text{rGO}$ nanohybrid by the Scherrer formula [34]. Two obvious diffraction peaks corresponding to (002) and (100) of carbon phase can be observed in rGO. The average crystallite size of pure CoFe_2O_4 is estimated to be 5.0 nm by the Scherrer formula, which is similar to that of CoFe_2O_4 nanoparticles in $\text{CoFe}_2\text{O}_4/\text{rGO}$ nanohybrid.

The morphology and structure of the $\text{CoFe}_2\text{O}_4/\text{rGO}$ was investigated by transmission electron microscope (TEM). As observed from Fig. 2a and b, CoFe_2O_4 nanoparticles were well dispersed on the graphene. The histogram of the CoFe_2O_4 particle size distribution in $\text{CoFe}_2\text{O}_4/\text{rGO}$ nanohybrid is in the range of 3.0–6.5 nm with an average particle size of 4.8 nm (Fig. 2a), in good agreement with the value obtained from XRD. The crystal structure of the CoFe_2O_4 particles on graphene was further revealed by high-resolution TEM. The measured d spacing of 0.29 nm is assigned to the lattice spacing of the (220) plane of CoFe_2O_4 (Fig. 2c). Fig. 2d exhibits the selected area electron diffraction (SAED) patterns of the CoFe_2O_4 on graphene. The five most-distinct concentric diffraction rings from the centre can be assigned to the (220), (311), (400), (511) and (440) planes of cubic spinel CoFe_2O_4 , which agrees well with the results obtained from the XRD pattern (Fig. 1). Note that the particle size of pure CoFe_2O_4 without any substrate is in the range of 10–20 nm as

shown in the SEM image (Fig. S1), which is larger than that of mean crystallite size calculated from Scherrer formula (5.0 nm) due to the aggregation of the particles. In contrast, the smaller particle size of CoFe_2O_4 nanoparticles in $\text{CoFe}_2\text{O}_4/\text{rGO}$ nanohybrid is due to the dispersing effect of graphene support in preventing the CoFe_2O_4 nanoparticles from aggregation.

To obtain the cation oxidation state and the surface chemical composition of CoFe_2O_4 on graphene, X-ray photoelectron spectroscopy (XPS) measurements were performed. As expected, the XPS survey spectrum given in Fig. 3a shows the Co 2p, Fe 2p, O 1s and C 1s peaks in CoFe_2O_4 on graphene. The de-convolution of the Co 2p peak in CoFe_2O_4 and $\text{CoFe}_2\text{O}_4/\text{rGO}$ shows four peaks (Fig. 3b). The peak at 780.7 eV is from $\text{Co}2p_{3/2}$, while the peak at 796.3 eV is caused by $\text{Co}2p_{1/2}$. The satellite peak at around 785.8 eV and 803.1 eV are two shake-up type peaks of Co at the high binding energy side of the $\text{Co}2p_{3/2}$ and $\text{Co}2p_{1/2}$ edge. The presence of $\text{Co}2p_{3/2}$ and $\text{Co}2p_{1/2}$ main peaks and shake-up satellite peaks indicates the presence of Co^{2+} in the high-spin state [35–37]. The Fe 2p spectra shows two peaks at a binding energy of around 710.9 eV and 724.2 eV, corresponding to $\text{Fe}2p_{3/2}$ and $\text{Fe}2p_{1/2}$, respectively, suggesting the presence of Fe^{3+} cations [35–37]. Further quantitative analysis of the Co 2p and Fe 2p peaks gave a Co:Fe atomic ratio of about 1:2, which is consistent with the results of XRD. The O 1s spectra in CoFe_2O_4 and $\text{CoFe}_2\text{O}_4/\text{rGO}$ show a large peak at 529.3 eV and 529.9 eV, respectively, corresponding to M–O–M, which is attributed to the lattice oxygen in the Co/Fe–oxygen framework [21,36–38]. The comparison of Co 2p and Fe 2p spectra in CoFe_2O_4 and $\text{CoFe}_2\text{O}_4/\text{rGO}$ has revealed no shift in the binding energy of the peaks after the hybridization of CoFe_2O_4 and graphene sheets (Fig. 3b and c). However, a positive shift of about 0.6 eV in the binding energy for the O 1s peak is observed for $\text{CoFe}_2\text{O}_4/\text{rGO}$ as compared to that of CoFe_2O_4 (Fig. 3d). This indicates that the

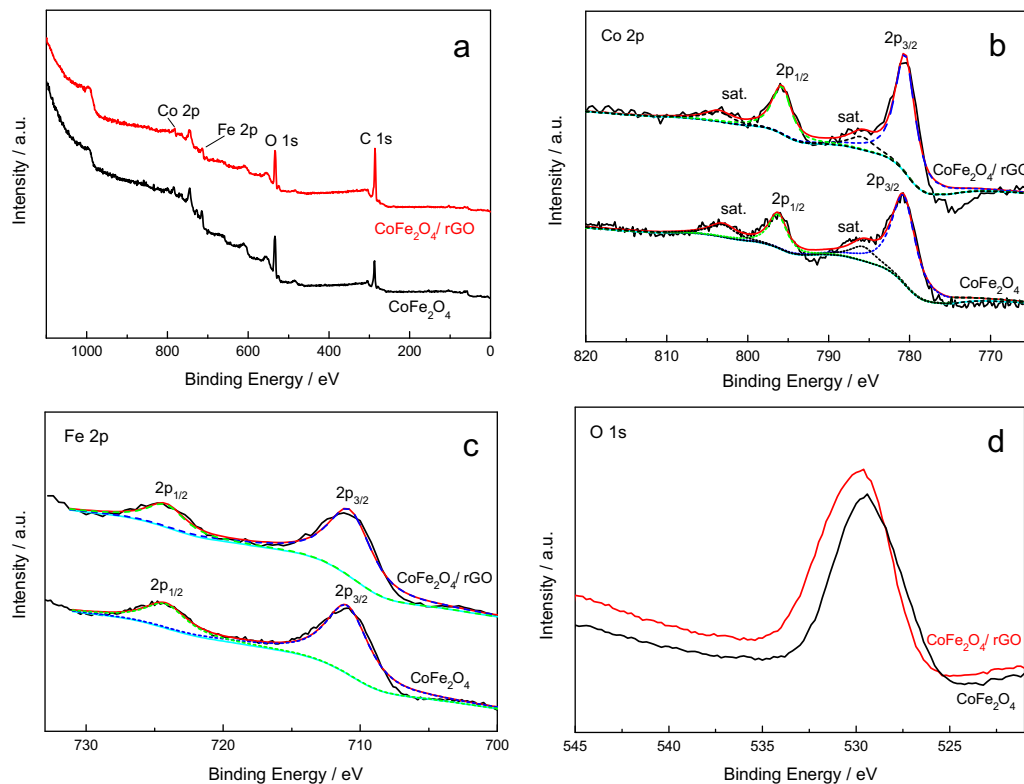


Fig. 3. (a) XPS survey spectra of $\text{CoFe}_2\text{O}_4/\text{rGO}$ nanohybrid and CoFe_2O_4 ; (b) XPS spectra for the Co 2p peak of $\text{CoFe}_2\text{O}_4/\text{rGO}$ and CoFe_2O_4 ; (c) XPS spectra for the Fe 2p peak of $\text{CoFe}_2\text{O}_4/\text{rGO}$ and CoFe_2O_4 ; (d) XPS spectra for the O 1s peak of $\text{CoFe}_2\text{O}_4/\text{rGO}$ and CoFe_2O_4 .

coupling between CoFe_2O_4 and graphene occurs through the oxygen species of GO, which probably reacted with the metal precursors during the synthesis [21].

The N_2 sorption isotherm and the pore size distribution of $\text{CoFe}_2\text{O}_4/\text{rGO}$ nanohybrid are shown in Fig. 4. The N_2 -adsorption isotherm of the $\text{CoFe}_2\text{O}_4/\text{rGO}$ exhibited type IV isotherm, the hysteresis loop in the P/P_0 range of 0.5–1.0 is indicative of mesoporosity. The $\text{CoFe}_2\text{O}_4/\text{rGO}$ displays a BET specific surface area of $173.12 \text{ m}^2 \text{ g}^{-1}$ and a total pore volume of $12.57 \text{ cm}^3 \text{ g}^{-1}$. A broad pore size distribution between 2 and 70 nm is clearly observed in Fig. 4b, which might come from the interlayer spacings and porous structure formed between graphene sheets. The high surface area of $\text{CoFe}_2\text{O}_4/\text{rGO}$ provides a high surface exposure of active sites for the ORR. Meanwhile, the broad pore size distribution provides effective triple phase (solid–liquid–gas) regions required for oxygen reduction. Note that the specific surface area of the $\text{CoFe}_2\text{O}_4/\text{rGO}$ nanohybrid is much lower than the theoretical value of graphene ($2630 \text{ m}^2 \text{ g}^{-1}$), which is due to the bigger weight contribution from CoFe_2O_4 nanoparticles on the surface of graphene sheets [39].

3.2. Catalytic activity of $\text{CoFe}_2\text{O}_4/\text{rGO}$ nanohybrid for oxygen reduction and oxygen evolution

The ORR activity on $\text{CoFe}_2\text{O}_4/\text{rGO}$ nanohybrid as measured with RRDE is shown in Fig. 5. To better understand the electrocatalytic

performance of $\text{CoFe}_2\text{O}_4/\text{rGO}$ during the ORR process, the ORR activities on CoFe_2O_4 (mixed with AB), rGO, $\text{CoFe}_2\text{O}_4 + \text{rGO}$ mixture and commercial Pt/C are also included for comparison. The disk current densities (I_D) shown were measured at 1600 rpm and normalized by the geometric surface area. The ORR activity increases as follows: $\text{CoFe}_2\text{O}_4 < \text{rGO} < \text{CoFe}_2\text{O}_4 + \text{rGO}$ mixture $< \text{CoFe}_2\text{O}_4/\text{rGO}$, as evidenced by the onset potentials for the ORR of these samples (Fig. 5a). The rGO has high electronic conductivity. The edge sites and defect sites of rGO prepared from graphite by a modified Hummer's method could serve as active sites for oxygen reduction. Meanwhile the two-dimensional structure of rGO allows the easy access of O_2 from both sides to these active sites [40]. These facts result in the higher ORR activity of $\text{CoFe}_2\text{O}_4 + \text{rGO}$ mixture than that of CoFe_2O_4 (mixed with AB). A significant increase in the onset potential for the ORR of $\text{CoFe}_2\text{O}_4/\text{rGO}$ (-0.136 V) as compared to that of $\text{CoFe}_2\text{O}_4 + \text{rGO}$ mixture (-0.207 V) is indicative of the important effect of hybridization of CoFe_2O_4 and graphene on the ORR activity. The diffusion limiting current density of $\text{CoFe}_2\text{O}_4/\text{rGO}$ reaches that of Pt/C though a negative shift of about 80 mV exists in the half-wave potential of $\text{CoFe}_2\text{O}_4/\text{rGO}$ as compared to Pt/C. It should be noted that the

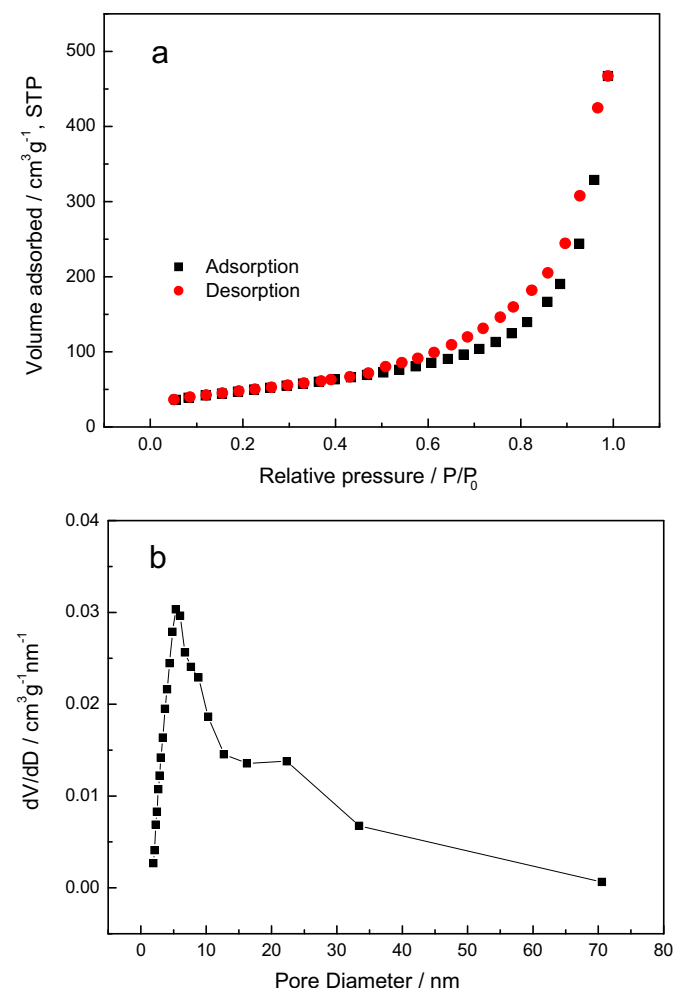


Fig. 4. BET surface area (a) and pore size distribution (b) for $\text{CoFe}_2\text{O}_4/\text{rGO}$ nanohybrid.

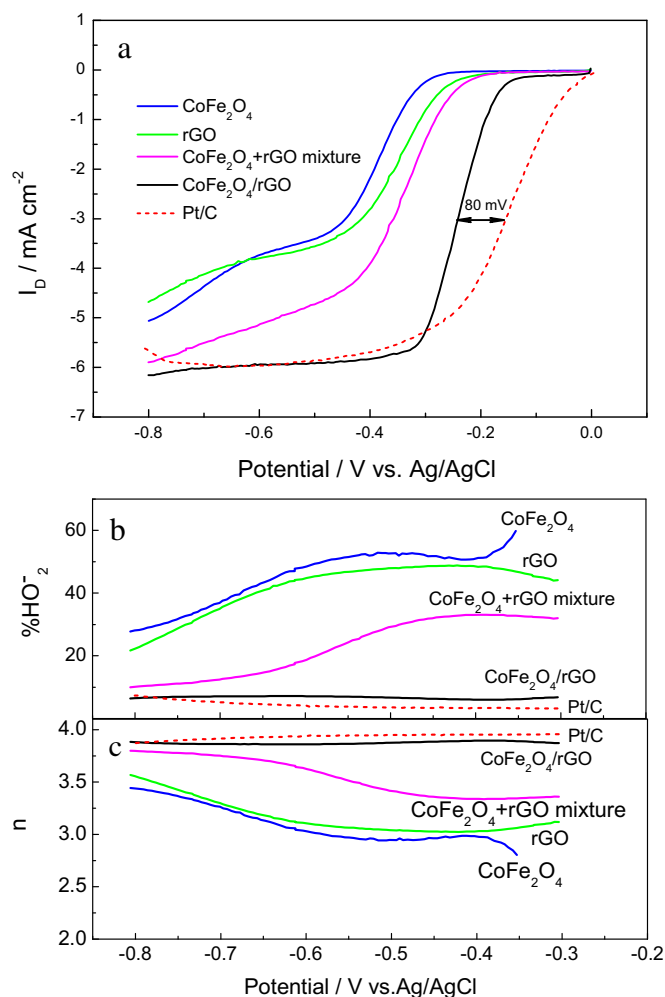


Fig. 5. (a) Linear sweeping voltammograms (LSVs) on rotating ring-disk electrode for CoFe_2O_4 (mixed with AB), rGO, $\text{CoFe}_2\text{O}_4 + \text{rGO}$ mixture and commercial Pt/C in O_2 -saturated 0.1 M KOH at a rotating speed of 1600 rpm. The disk potential was scanned at 10 mV s^{-1} and the ring potential was fixed at 0.5 V. (b) Calculated electron transfer number n and (c) determined peroxide percentage at various potentials based on the corresponding RRDE data in (a).

diffusion limiting current density and half-wave potential of the Pt/C are in good agreement with the values of Pt/C (20 wt% Pt) reported elsewhere [41,42]. To verify the ORR catalytic pathways of the catalysts, the formation of peroxide species (HO_2^-) during the ORR process was monitored with RRDE measurements (Fig. 5b). The measured HO_2^- yield on the catalysts decreases as follows: $\text{CoFe}_2\text{O}_4 > \text{rGO} > \text{CoFe}_2\text{O}_4 + \text{rGO mixture} > \text{CoFe}_2\text{O}_4/\text{rGO}$, the corresponding electron number transferred during the ORR reaction decreases in the reverse order. The measured HO_2^- yield is 27–60% for CoFe_2O_4 , and it significantly decreases to below $\sim 10\%$ for $\text{CoFe}_2\text{O}_4/\text{rGO}$ nanohybrid over the potential range of -0.80 to -0.30 V, giving an electron transfer number of 3.84–3.90. This is comparable to Pt/C, HO_2^- yield for which is below $\sim 8\%$ and electron transfer number for which is 3.90–3.96 (Fig. 5b and c). These results indicate that the hybridization of CoFe_2O_4 and graphene not only significantly improves the catalytic activity of CoFe_2O_4 but also modifies the ORR catalytic pathway. Furthermore, the improved catalytic activity and quasi-4-electron pathway of $\text{CoFe}_2\text{O}_4/\text{rGO}$ nanohybrid as compared to that of $\text{CoFe}_2\text{O}_4 + \text{rGO}$ mixture suggests that coupling between CoFe_2O_4 and rGO through oxygen species in GO during the synthesis (Fig. 5d) plays an important role in improving the catalytic activity and modifying the catalytic pathway of CoFe_2O_4 towards ORR. The high activity of $\text{CoFe}_2\text{O}_4/\text{rGO}$ nanohybrid is attributed to the following factors. First, in contrast to $\text{CoFe}_2\text{O}_4 + \text{rGO}$ mixture (loose contact could be expected), the coupling between CoFe_2O_4 and rGO in $\text{CoFe}_2\text{O}_4/\text{rGO}$ nanohybrid renders an intimate contact of CoFe_2O_4 and rGO and facilitates more efficient electronic conduction, which benefits reaction kinetics and CoFe_2O_4 utilization. Second, the high dispersion of CoFe_2O_4 particles on rGO resulting from the coupling between CoFe_2O_4 and rGO provides high surface area and also can shorten the diffusion path of ions, such as OH^- and the reaction intermediates HO_2^- . Third, the two-dimensional structure of rGO allows the easy access of O_2 from both sides to active sites as well as electrolyte accessibility. The CoFe_2O_4 (mixed with AB) and rGO exhibit similar hydrogen peroxide yields. The $\text{CoFe}_2\text{O}_4 + \text{rGO}$ mixture shows lower peroxide yields than that of CoFe_2O_4 (mixed with AB), which is due to the efficient reduction of O_2 on the edge sites and defect sites on both sides of two-dimensional structure of rGO. The quasi-4-electron pathway (i.e. peroxide yields of below $\sim 10\%$) of $\text{CoFe}_2\text{O}_4/\text{rGO}$ towards ORR is mainly ascribed to the high electronic conduction caused by the coupling between CoFe_2O_4 and rGO in $\text{CoFe}_2\text{O}_4/\text{rGO}$ nanohybrid. Lee's studies on the ORR activity of $\text{rGO}/\text{Mn}_3\text{O}_4$ have shown that it can change from 4-electron pathway to 2-electron pathway as the relative amount of Mn_3O_4 increases from 10% to 50% in $\text{rGO}/\text{Mn}_3\text{O}_4$. This shows that high content of Mn_3O_4 with respect to rGO results in lower electrical conductivity and therefore an adverse effect on the catalytic pathway [43].

The diffusion-current-corrected Tafel plots of specific ORR activity of these samples are shown in Fig. 6. To construct the Tafel plots, the kinetic currents were derived from the mass-transport correction using Eq. (2). At low over-potentials, the Tafel slope is 75, 79, 78 and 67 mV dec^{-1} for CoFe_2O_4 (mixed with AB), rGO, $\text{CoFe}_2\text{O}_4 + \text{rGO}$ mixture and $\text{CoFe}_2\text{O}_4/\text{rGO}$ nanohybrid, respectively. The Tafel slope of $\text{CoFe}_2\text{O}_4/\text{rGO}$ (67 mV dec^{-1}) is smaller than that of CoFe_2O_4 , rGO and $\text{CoFe}_2\text{O}_4 + \text{rGO}$ mixture, and is close to that of Pt/C (69 mV dec^{-1}). It approaches the theoretical value of $2.303RT/F$ (i.e., 59 mV dec^{-1} at 25°C), where R is the universal gas constant, F is the Faraday constant, and T is absolute temperature. The low Tafel slope indicates the high intrinsic catalytic activity of $\text{CoFe}_2\text{O}_4/\text{rGO}$ nanohybrid.

The polarization curves for the ORR on $\text{CoFe}_2\text{O}_4/\text{rGO}$ nanohybrid at different rotation rates are shown in Fig. 7. They all reached well-defined diffusion limiting currents. The inset in Fig. 7 shows the

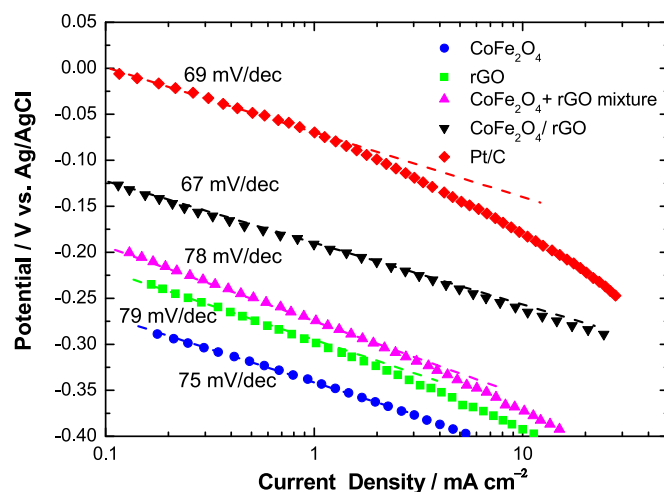


Fig. 6. Tafel plots of CoFe_2O_4 (mixed with AB), rGO, $\text{CoFe}_2\text{O}_4 + \text{rGO}$ mixture, $\text{CoFe}_2\text{O}_4/\text{rGO}$ nanohybrid and commercial Pt/C derived by the mass-transport correction of corresponding LSV data recorded in O_2 -saturated 0.1 M KOH with a sweeping rate of 10 mV s^{-1} and a rotating speed of 1600 rpm.

corresponding Koutecky–Levich plots obtained from the inverse current density (j^{-1}) as a function of the inverse of the square root of the rotation rate ($\omega^{-1/2}$) for $\text{CoFe}_2\text{O}_4/\text{rGO}$ at -0.22 , -0.23 , -0.25 and -0.36 V, respectively. These plots are linear and parallel, indicating the first-order dependence of the kinetics of ORR on the $\text{CoFe}_2\text{O}_4/\text{rGO}$ surface. Each straight line intercept corresponds to the kinetic current i_k . The “B-factor” for $\text{CoFe}_2\text{O}_4/\text{rGO}$ is $0.147 \text{ mA cm}^{-2} \omega^{-1/2}$, determined from the slope of Koutecky–Levich plots. The electron number n calculated from the B-factor is in the range of 3.85–3.94. This is consistent with the result ($n \approx 3.84 - 3.90$) obtained from the RRDE measurements, suggesting that $\text{CoFe}_2\text{O}_4/\text{rGO}$ favours $4e^-$ reduction reaction process.

The catalytic activity of $\text{CoFe}_2\text{O}_4/\text{rGO}$ nanohybrid for the oxygen evolution reaction (OER) was also investigated. Fig. 8 shows the anodic linear scanning voltammograms for the OER on $\text{CoFe}_2\text{O}_4/\text{rGO}$, $\text{CoFe}_2\text{O}_4 + \text{rGO}$ mixture, rGO, CoFe_2O_4 (mixed with AB) and commercial Pt/C catalysts in N_2 -saturated 0.1 M KOH solution at a

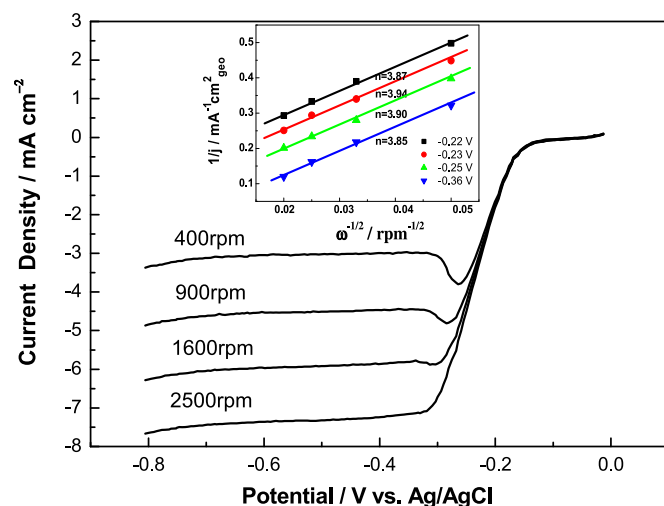


Fig. 7. LSVs of $\text{CoFe}_2\text{O}_4/\text{rGO}$ nanohybrid in O_2 -saturated 0.1 M KOH with a scan rate of 10 mV s^{-1} at different rotating speeds. Inset: Koutecky–Levich plots for ORR in O_2 -saturated 0.1 M KOH solution for $\text{CoFe}_2\text{O}_4/\text{rGO}$.

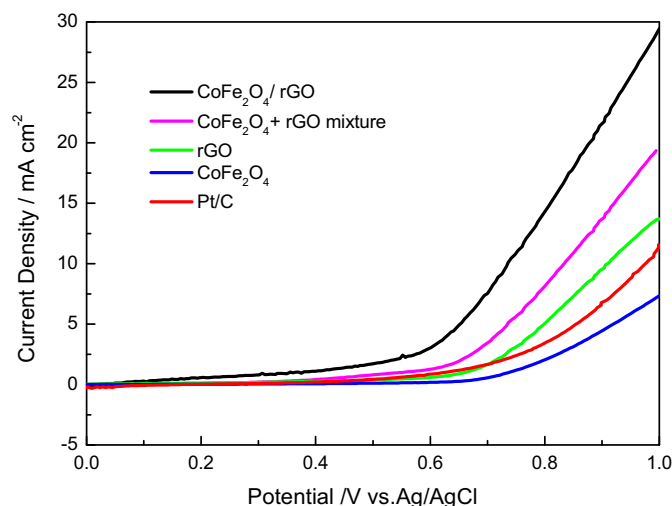


Fig. 8. Anodic linear scanning voltammograms for the OER on CoFe₂O₄ (mixed with AB), rGO, CoFe₂O₄ + rGO mixture, CoFe₂O₄/rGO nanohybrid and commercial Pt/C in O₂-saturated 0.1 M KOH with a sweeping rate of 10 mV s⁻¹ and a rotating speed of 1600 rpm.

rotation speed of 1600 rpm. The CoFe₂O₄ + rGO mixture exhibits lower onset potential (0.62 V) and higher current density (19.4 mA cm⁻²) for the OER than CoFe₂O₄ (mixed with AB). Similar to ORR, the edge sites and defect sites of rGO are active sites for OER and the two-dimensional structure of rGO allows the easy transfer of electrolyte/O₂ on both sides to/away active sites. Note that the activity of Pt/C is only slightly higher than that of CoFe₂O₄ and lower than that of the other three catalysts. This clearly shows that Pt/C is not a good catalyst for OER, which agrees well with the results reported by Liang et al. [11]. The OER activity is further improved on CoFe₂O₄/rGO nanohybrid, the onset potential on which is 0.54 V and the current density on which is 29.5 mA cm⁻². The high catalytic activity of CoFe₂O₄/rGO suggests that CoFe₂O₄/rGO is a promising bi-functional electrocatalyst for the ORR and OER. The results indicate the coupling between CoFe₂O₄ and rGO and the triple phase (solid–liquid–gas) region formed in CoFe₂O₄/rGO nanohybrid (similar to ORR) required for transport of reactants and products during the process of OER are important for the high activity of CoFe₂O₄/rGO nanohybrid.

The stabilities of CoFe₂O₄/rGO, CoFe₂O₄ (mixed with AB), rGO and commercial Pt/C catalysts for the ORR and the OER were examined with the chronoamperometric method in O₂-saturated 0.1 M KOH at 1600 rpm as shown in Fig. 9. The ORR current density of CoFe₂O₄ and rGO at -0.8 V decreases by 16.7% and 15.0%, respectively, after 43,200 s continuous operation, while a decrease of only 5.5% in current density is observed for the CoFe₂O₄/rGO catalyst (Fig. 9a). The worst case is Pt/C, the ORR current density of which decreases 52.4% after 43,200 s. For the OER stability, CoFe₂O₄/rGO catalyst shows a decrease of 8.7% in current density at 0.8 V after 43,200 s, which is much lower than that of CoFe₂O₄ (16.4%) and rGO (25.9%), respectively. And Pt/C degraded much more severely, showing a decrease of 71.3% in the OER current density after 43,200 s. It's noticed that rGO exhibits more current decay in OER than in ORR, which is probably due to the oxidation of carbon at high potentials as reported by other groups [44,45]. The results reveal that the CoFe₂O₄/rGO nanohybrid is quite stable for both the ORR and OER, which most likely results from the strong coupling between CoFe₂O₄ and rGO. The strong coupling between CoFe₂O₄ and rGO prevents detachment and aggregation of CoFe₂O₄ during the process of ORR and OER, which improves the electrode cyclic stability.

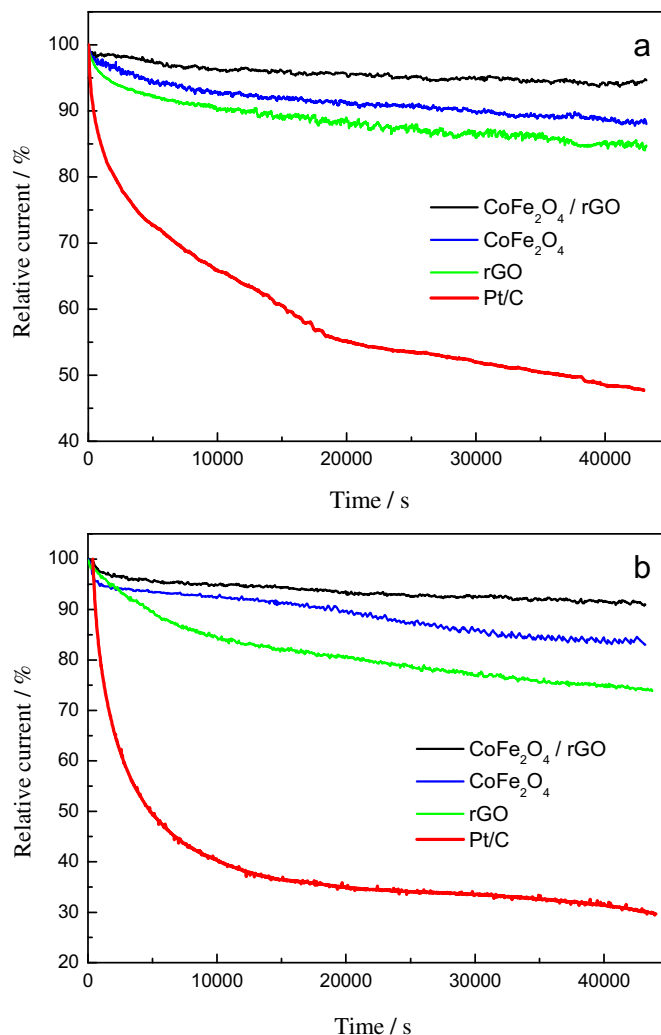


Fig. 9. Current–time (*i*–*t*) chronoamperometric responses for the ORR (a) and the OER (b) on CoFe₂O₄ (mixed with AB), rGO, CoFe₂O₄/rGO nanohybrid and commercial Pt/C in O₂-saturated 0.1 M KOH at -0.4 V (vs. Ag/AgCl) for ORR and in N₂-saturated 0.1 M KOH at 0.8 V (vs. Ag/AgCl) for OER at a rotating speed of 1600 rpm.

4. Conclusions

In summary, CoFe₂O₄/rGO nanohybrid electrocatalysts were prepared via a two-step process. The CoFe₂O₄/rGO nanohybrid has shown high activity for the ORR in alkaline solutions and a four electron pathway is dominant for the ORR. Furthermore, high catalytic activity of CoFe₂O₄/rGO catalyst for the OER has also been demonstrated. This shows that CoFe₂O₄/rGO catalyst simultaneously owns promising catalytic activity for both the ORR and the OER. Meanwhile, the CoFe₂O₄/rGO is found to be quite stable for both the ORR and the OER, outperforming the commercial Pt/C. The improvement in the catalytic activity and stability in the CoFe₂O₄/rGO for the ORR and the OER mainly arises from the strong coupling between CoFe₂O₄ and rGO. The results indicate that CoFe₂O₄/rGO nanohybrid could be used as a potential bi-functional catalyst for metal–air batteries.

Acknowledgements

This work is supported by National Natural Science Foundation of China (Nos. 51272167 and 21206101), Natural Science Foundation of the Higher Education Institutions of Jiangsu Province, China

(12KJB430010). Part of this work is supported by Sino-German Network on Electromobility.

Appendix A. Supplementary data

Supplementary data related to this article can be found at <http://dx.doi.org/10.1016/j.jpowsour.2013.11.024>.

References

- [1] R.R. Adzic, in: J. Lipkowski, P.N. Ross (Eds.), *Electrocatalysis*, Wiley, New York, 1998, p. 197.
- [2] M. Armand, J.M. Tarascon, *Nature* 451 (2008) 652.
- [3] P.G. Bruce, L.J. Hardwick, K.M. Abraham, *Mater. Res. Soc. Bull.* 36 (2011) 506.
- [4] V. Neburchilov, H.J. Wang, J.J. Martin, W. Qu, *J. Power Sources* 195 (2010) 1271.
- [5] H.A. Gasteiger, S.S. Kocha, B. Sompalli, F.T. Wagner, *Appl. Catal. B* 9 (2005) 56.
- [6] F.Y. Cheng, J. Chen, *Chem. Soc. Rev.* 41 (2012) 2172.
- [7] J. Suntivich, H.A. Gasteiger, N. Yabuuchi, H. Nakanishi, J.B. Goodenough, Y. Shao-Horn, *Nat. Chem.* 3 (2011) 546.
- [8] J. Suntivich, K.J. May, H.A. Gasteiger, J.B. Goodenough, Y. Shao-Horn, *Science* 334 (2011) 1383.
- [9] M. Hamdani, R.N. Singh, P. Chartier, *Int. J. Electrochem. Sci.* 5 (2010) 556.
- [10] F.Y. Cheng, J. Shen, B. Peng, Y.D. Pan, J. Chen, *Nat. Chem.* 3 (2011) 79.
- [11] Y.Y. Liang, Y.G. Li, H.L. Wang, J.G. Zhou, J. Wang, T. Regier, H.J. Dai, *Nat. Mater.* 10 (2011) 780.
- [12] L. Wang, X. Zhao, Y. Lu, M. Xu, D. Zhang, R.S. Ruoff, K.J. Stevenson, J.B. Goodenough, *J. Electrochem. Soc.* 158 (2011) A1379.
- [13] Y.Y. Liang, H.L. Wang, J.G. Zhou, Y.G. Li, J. Wang, T. Regier, H.J. Dai, *J. Am. Chem. Soc.* 134 (2012) 3517.
- [14] M.D. Koninck, S.C. Poirier, B. Marsan, *J. Electrochem. Soc.* 153 (2006) A2103.
- [15] M.D. Koninck, S.C. Poirier, B. Marsan, *J. Electrochem. Soc.* 154 (2007) A381.
- [16] X.Z. Yuan, W. Qu, J. Fahlman, *ECS Trans.* 45 (2013) 105.
- [17] I. Nikolov, R. Darkaout, E. Zhecheva, R. Stoyanova, N. Dimitrov, T. Vitamov, *J. Electroanal. Chem.* 429 (1997) 157.
- [18] Y. Zhu, S. Murali, W. Cai, X. Li, J.W. Suk, J.R. Potts, R.S. Ruoff, *Adv. Mater.* 22 (2010) 3906.
- [19] G. Eda, M. Chhowalla, *ACS Nano* 5 (2011) 4265.
- [20] X. Huang, X.Y. Qi, F. Boey, H. Zhang, *Chem. Soc. Rev.* 41 (2012) 666.
- [21] D.U. Lee, B.J. Kim, Z.W. Chen, *J. Mater. Chem. A* 1 (2013) 4754.
- [22] E. Laouini, J. Douch, M. Hamdani, Y. Berghoute, M.H. Mendonça, M.I.S. Pereira, R.N. Singh, *J. Appl. Electrochem.* 41 (2011) 731.
- [23] E. Laouini, Y. Berghoute, J. Douch, M.H. Mendonça, M. Hamdani, M.I.S. Pereira, *J. Appl. Electrochem.* 39 (2009) 2469.
- [24] M.A.M. Cartaxo, T.A.S. Ferreira, M.R. Nunes, H. Mendonça, M.L. da Silva Pereira, F.M. Costa, *Solid State Sci.* 9 (2007) 744.
- [25] W.S. Hummers, R.E. Offeman, *J. Am. Chem. Soc.* 80 (1958) 1339.
- [26] D.A. Shirley, *Phys. Rev. B* 5 (1972) 4709.
- [27] D. Briggs, M.P. Seah, *Practical Surface Analysis*, Wiley Interscience, New York, 1990.
- [28] N.M. Markovic, H.A. Gasteiger, P.N. Ross, *J. Phys. Chem.* 100 (1996) 6715.
- [29] H. Meng, F. Jaouen, E. Proietti, M. Lefèvre, J.-P. Dodelet, *Electrochem. Commun.* 11 (2009) 1986.
- [30] D.R. Lide, *CRC Handbook of Chemistry and Physics*, CRC Press, Boca Raton, FL, 1995.
- [31] J. Sunarso, A.A. Torriero, W. Zhou, P.C. Howlett, M. Forsyth, *J. Phys. Chem. C* 116 (2012) 5827.
- [32] J. Du, Y.D. Pan, T.R. Zhang, X.P. Han, F.Y. Cheng, J. Chen, *J. Mater. Chem.* 22 (2012) 15812.
- [33] N.M. Markovic, T.J. Schmidt, V. Stamkovic, P.N. Ross, *Fuel Cells* 105 (2001) 1.
- [34] V. Radmilovic, H.A. Gasteiger, P.N. Ross Jr., *J. Catal.* 154 (1995) 98.
- [35] H.L. Yuan, Y.Q. Wang, S.M. Zhou, L.S. Liu, X.L. Chen, S.Y. Lou, R.J. Yuan, Y.M. Hao, N. Li, *Nanoscale Res. Lett.* 5 (2010) 1817.
- [36] G.B. Ji, S.L. Tang, S.K. Ren, F.M. Zhang, B.X. Gu, Y.W. Du, *J. Cryst. Growth* 270 (2004) 156.
- [37] G.C. Allen, S.J. Harris, J.A. Jutson, J.M. Dyke, *Appl. Surf. Sci.* 37 (1989) 111.
- [38] Y. Sharma, N. Sharma, G.V. Subba Rao, B.V.R. Chowdari, *Solid State Ionics* 179 (2008) 587–597.
- [39] Z. Ji, X. Shen, G. Zhu, H. Zhou, A. Yuan, *J. Mater. Chem.* 22 (2012) 3471.
- [40] E. Yoo, H.S. Zhou, *ACS Nano* 5 (2011) 3020.
- [41] L. Jiang, A. Hsu, D. Chu, R. Chena, *J. Electrochem. Soc.* 156 (2009) B370.
- [42] W. Yang, T.-P. Fellinger, M. Antonietti, *J. Am. Chem. Soc.* 133 (2011) 206.
- [43] J.-S. Lee, T. Lee, H.-K. Song, J. Cho, B.-S. Kim, *Energy Environ. Sci.* 4 (2011) 4148.
- [44] S.A. Freunberger, Y. Chen, N.E. Drewett, L.J. Hardwick, F. Barde, P.G. Bruce, *Angew. Chem. Int. Ed* 50 (2011) 8609.
- [45] B.M. Gallant, R.R. Mitchell, D.G. Kwabi, Z.L. Zhou, C.V. Thompson, Y. Shao-Horn, *J. Phys. Chem. C* 116 (2012) 20800.